Geochemical and geomechanical alteration of siliciclastic reservoir rock by supercritical CO_2-saturated brine formed during geological carbon sequestration

Samantha J. Fuchs[a], D. Nicholas Espinoza[b], Christina L. Lopano[c], C., Ange-Therese Akono[d], and Charles J. Werth[a*]

a) Department of Civil, Architecture and Environmental Engineering, University of Texas at Austin, 301 East Dean Keeton St., Austin, TX 7872. sfuchs@utexas.edu, werth@utexas.edu

b) Department of Petroleum and Geosystems Engineering, University of Texas at Austin, 200 E Dean Keeton St., TX 78721. espinoza@austin.utexas.edu

c) Office of Research and Development, US DOE - National Energy Technology Laboratory, 626 Cochrans Mill Road, P.O. Box 10940, Pittsburgh, PA 15236. Christina.Lopano@netl.doe.gov

d) Department of Civil and Environmental Engineering, Northwestern University, 2145 Sheridan Road, Evanston, IL 60208. ange-therese.akono@northwestern.edu

* Corresponding Author: werth@utexas.edu, 217-377-6063

Abstract

Geologic carbon sequestration (GCS) is an approach for storing CO_2 and mitigating greenhouse gas emissions. During GCS, carbon dioxide dissolves into pore water, resulting in a low-pH brine that can react with reservoir rock minerals. This work evaluates the effects of geochemical reactions on geomechanical integrity of representative siliciclastic reservoir samples obtained from the Mt. Simon formation. Rock samples were aged 4 or 8 weeks in CO_2-saturated brine under reservoir conditions, and in N_2-saturated brine as a control. Post-aging, CT scans revealed more extensive micro-fracture development along horizontal bedding planes at grain edges in CO_2 versus N_2-aged samples. Digital analysis of CO_2-aged samples showed porosity increase from 8.1% to 15.8%. Scanning electron microscopy revealed the loss of clay cementation, greater exposure of quartz and K-feldspar grains, and apparent surface roughening (confirmed by laser profilometry) in CO_2-aged samples, but not in N_2-aged samples. Fracture toughness as evaluated by scratch testing was reduced by 32.1% after 4 weeks in scCO_2-saturated brine and 69.5% after 8 weeks. The primary reason for weakening appears to be detachment of clays from quartz and feldspar grain surfaces, resulting in weakening of the rock matrix. Rock weakening may alter the geomechanical stability of storage formations.

Keywords: geologic carbon sequestration; geochemistry; geomechanics; Mt. Simon, fracture toughness

1. Introduction

Carbon dioxide is a potent greenhouse gas that has been directly linked to anthropogenic climate change [1]. Capturing and storing carbon dioxide was proposed as an essential mitigation approach to prevent further rise of atmospheric CO_2 concentrations. Geologic carbon sequestration has emerged as a promising technique because of the large potential capacity to store CO_2 in deep underground formations. The process involves taking CO_2 captured at a stationary source, such as a power plant or a refinery, and injecting it into deep saline formations and oil and gas fields. A key concern of geologic carbon sequestration is that injected CO_2 may induce felt seismic events, and possibly harm surface structures or induce fracturing of caprock seals [2], [3]. Injected CO_2 dissolves into pore water as carbonic acid, and can react with pore water constituents and minerals to promote dissolution and precipitation reactions. A critical knowledge gap is the impact of these reactions on geomechanical properties such as fracture toughness and on potential seismic activity.

Multiple studies have investigated geochemical reactions between CO_2, brine and reservoir rocks, using both static batch and dynamic core-flood experiments [4]. The concentration of carbonic acid in brine is markedly higher under supercritical conditions found in many reservoirs, resulting in pH values as low as 4.3 [5]. Lower pH conditions can dissolve numerous minerals, and in some cases results in secondary mineral precipitation. Both batch and core-flood experiments have shown that particularly reactive mineral end members like calcite or dolomite readily dissolve in low pH solutions [6], [7], and that less reactive minerals like hematite, K-feldspar, and clays (e.g., illite) also dissolve, but at slower rates [7]–[9]. Various numerical modeling approaches have been used to evaluate precipitation and dissolution reactions during carbon sequestration, in some cases with good agreement to experiments [6],

[11]–[15]. Considering the extended time of CO_2 sequestration, all dissolution reactions are likely relevant and may impact reservoir geomechanical integrity.

Reactive minerals can serve as cementation agents that bind larger and less-reactive grains together. Feldspars and clays serve as primary binding agents in siliciclastic reservoirs [5]; however, cementation can be a complex process, including multiple cementing regimes with different reactivity at low pH, such as calcite and quartz [16], [17]. Digital image analyses via Scanning Electron Microscopy (SEM) and thin section analysis have indicated that dissolution of mineral cementation agents (e.g., clays, carbonates) can occur in reservoir samples exposed to CO_2-saturated brine [18]. Dissolution reactions can increase porosity and permeability [18], [19], which can create preferential flow channels, leading to further reactions, especially along these flow paths or faults; however, dissolution reactions can also result in mobilization of fines, which can reduce reservoir permeability [20]–[22]. Dissolution of cementitious minerals is generally expected to decrease geomechanical integrity, but concurrent processes make predictions uncertain.

Secondary mineral precipitation has been observed in heterogeneous reservoir samples exposed to CO_2 under supercritical conditions. For example, phyllosilicate clay dissolution and formation of nanoparticulate amorphous silica and kaolinite were observed by using phlogopite (a phyllosilicate rock) as a clay surrogate under supercritical conditions in 1 M NaCl brine [23]. In this case, the precipitates formed at the location of dissolution before they mobilized and aggregated. Also, weathering of k-feldspar, albite, and dolomite cements in a European Buntner Sandstone under supercritical conditions (60°C, 15 MPa pore pressure) led to precipitation of montmorillonite, although dissolution was the dominant geochemical reaction observed in the short term (i.e., weeks) [5]. Secondary mineral formation of carbonates contributes to long-term

86 sequestration of carbon in reservoirs, based on numerical simulations for tens to thousands of
87 years [11], [19], [24]–[26]. This precipitation can also affect geomechanical properties. For
88 example, fast precipitation of carbonate has been shown to block pores and increase strain in a
89 rock matrix, possibly leading to fracturing [27].

90 The effects of geochemical reactions on geomechanical properties in carbon sequestration
91 reservoirs have received little attention until recently [28]–[30]. Reservoirs with preexisting
92 faults or fracture networks have been modeled over geological time scales considering pressure
93 gradients to evaluate cap rock integrity [31], [32], rather than upscaling models for chemical
94 reactions that may affect faults. In enhanced oil recovery, studies on the effects of supercritical
95 carbon dioxide injection focused on wellbore integrity, injection pressure, and reservoir
96 conditions that could lead to fault reactivation or compromised cap rock integrity [33]. In more
97 recent years, investigations have progressed to chemo-mechanic changes in strength, stiffness,
98 and fracture toughness in carbonate-bearing sandstones [21–23] and carbonate-bearing caprocks
99 [37]. When carbonate and clay containing sandstones are studied, the carbonate dissolution and
100 resulting weakening overshadows the reactions with clays [38]. Such strength decreases may
101 promote slip events during CO_2 injection [2], most likely along preferential flow pathways or
102 faults where cementitious minerals underwent dissolution. In general, the linking of geochemical
103 reactions in sandstones, particularly those of clay cements, to geomechanical properties
104 following geologic carbon sequestration is limited and complicated by the varied geological and
105 mechanical conditions of the reservoir [14].

106 The objectives of this work are to study the geochemical reactions that occur in a
107 representative siliciclastic storage reservoir during CO_2 sequestration, and determine if these
108 reactions weaken reservoir rock and make it more prone to suffer damage. The study uses

samples of the Mt. Simon Sandstone formation, the site of a pilot CO_2 injection project, where 1 million metric tons of CO_2 were injected between 2011 and 2014 [39]. Extensive microseismic activity was observed during and after CO_2 injection into the Mt. Simon reservoir [40], [41] despite injection pressures remaining below fracture pressures [42]. Samples of the Mt. Simon sandstone were aged in CO_2 and N_2-saturated brine under reservoir conditions, i.e., 52°C and 22 MPa (3190 psi). Before and after sample aging, computed tomography X-ray scanning (CT scan), optical microscopy, scanning electron microscopy (SEM), energy dispersive spectroscopy (EDS), and laser profilometry were used to quantify changes in structure, surface mineralogy and roughness. Geomechanical scratch tests were performed to measure changes in sample fracture toughness which were related to changes in sample mineralogy.

2. Materials

CO_2 99.5% purity (Praxair) was used for all experiments. Synthetic brine was composed of ultrapure, deionized water (resistivity 18 MΩ·cm) and sodium chloride (Alfa Aesar, 99%), calcium chloride (Sigma Aldrich, 99%), magnesium chloride (Sigma Aldrich, 99%), potassium chloride (MP Biomedicals, 99%), potassium bromide (Alfa Aesar, 99%), lithium chloride (Alfa Aesar, 99.9%), strontium chloride (Strem Chemicals, %), and borax (MP Biomedicals, 99%). The synthetic brine composition is based on the Mt. Simon formation pore water and is 208.7 g/L TDS, primarily consisting of NaCl (111.662 g/L, 1.911 M) and $CaCl_2{\cdot}2H_2O$ (78.3458 g/L, 0.533 M). The full composition is given as supplementary information in Table S1.

2.1 Rock Core Samples

Mt. Simon core sections were obtained from verification well #1 at the Illinois Basin Decatur site under the direction of the Geological Sequestration Consortium. A 3-in diameter, 6-

in long core was taken from a depth of 2111.35 m (6927 ft). The CO_2 injection zone was 2128-2148 m (6984-7050 ft) [43]; thus, it is highly unlikely that CO_2 contacted the core material during injection.

The mineralogical make-up of the Mt. Simon formation from nearby depth intervals was previously determined using X-ray dispersive spectroscopy (XRD) and scanning electron microscopy (SEM) coupled to energy dispersive spectroscopy (EDS). The minerals present at the 2118.4 m (6950 ft) interval include quartz (79%), potassium feldspar (K-feldspar, 15%), sericite (1%), illite-smectite (4%), iron oxide-illite (1%), and other trace minerals [43]. In the formation, quartz and feldspar contents were reported ranging from 40-80% and 13-22%, respectively, with clays content reaching as high as 28% for different samples between depths of 2082.7 to 2131.5 m (6833 to 6993 ft) [43].

2.2 Rock Sample Preparation

The Mt. Simon core section was cut into 1.9 cm tall, 2.54 cm wide, and 3.81 cm long samples (0.75 in tall, 1 in long, and 1.5 in long) using a low speed diamond wheel saw (South Bay Technology Inc., Model 650) with a 10:1 dilution of deionized water to lubricant oil (Johnson Brothers, Lube Cool, LC-16). Sample dimensions were chosen to fit the high-pressure and temperature reactor. During cutting, the high porosity layers of the heterogeneous core were observed to be more friable than lower porosity areas, so samples were handled gently to prevent sample degradation. After cutting, samples were rinsed with ethanol (ACS grade, Pharmco-Aaper), and dried in an oven for 24 hours at 50°C. Standard thin sections (30 μm thick) were prepared from samples at the Thin Section Laboratory in the Jackson School of Geosciences at UT Austin to evaluate heterogeneity in the grain structure. Each sample used for thin section

154 analysis was vacuum impregnated with blue epoxy (EpoThin Epoxy Hardener and Resin,
155 Bueller) to aid in identification of pore spaces.
156
157 **3. Experimental Methods**
158 *3.1 Reactor Setup and Operation*
159 Four different samples cut from the core material were exposed to reservoir conditions in
160 a custom-built high-pressure and temperature stainless-steel reactor [44]. The reactor was
161 initially a viewing cell, with sapphire windows allowing for ongoing visualization of the sample.
162 For each experiment, a 0.75x1x1.5-inch^3 sample was put into a custom glass sample holder and
163 placed into the reactor. The vessel was first flushed with CO_2 or N_2 to remove oxygen, heated to
164 52°C, and then filled with pre-equilibrated brine from a stainless-steel high-pressure vessel
165 (Hawk Valve, HiP model series OC). A syringe pump (Teledyne, model 500D) set at constant
166 pressure control was used to inject CO_2 or N_2 over 45 minutes to reach 3190 psi (22 MPa). The
167 selected temperature and pressure are similar to those in the Mt. Simon formation at 7033 ft, i.e.,
168 50°C, 22.1 MPa [45]. Experiments were run for 4 or 8 weeks in either N_2 or scCO_2-saturated
169 brine for sample aging. After each aging period, the reactor was gradually vented (i.e.,
170 depressurized) over 30 minutes, cooled, and drained for 10 mL brine collection. The reactor was
171 then taken apart, cleaned, dried, and reassembled to avoid the buildup of salts. Samples were
172 rinsed in ethanol and allowed to fully dry before removal from the sample holder due to fragility
173 when wetted.
174 **Table 1:** Sample Identities, experimental conditions, and selected techniques presented

Sample depth	ID	Aging Condition	Time	CT	SEM	Profilometry	Scratch Test
6927 ft	MS1	CO_2	Initial		X	X	X
	MS1	CO_2	4 weeks		X	X	X
	MS1	CO_2	8 weeks		X	X	

	MS2	CO_2	Initial	X			X
	MS2	CO_2	4 weeks				X
	MS2	CO_2	8 weeks	X			X
	MS3	N_2	Initial		X		X
	MS3	N_2	4 weeks		X		X
	MS4	N_2	Initial			X	X
	MS4	N_2	4 weeks			X	X
	MS4	N_2	8 weeks	X		X	X

All sample names, aging conditions, and associated characterization tests are listed in Table 1. Replicate experiments were performed for samples aged in either N_2 (MS3, MS4) or $scCO_2$ (MS1, MS2) saturated brine for 4 weeks, and for samples aged in $scCO_2$–saturated brine for a total of 8 weeks (MS1, MS2). Samples aged for 8 weeks were aged for two sequential 4-week periods and analyzed in between. All samples removed from the reactor after aging were rinsed with ethanol and dried in an oven for 24 hours at 50°C before analysis. The experimental preparation, with cooling, rinsing, and drying events, clearly deviate from reservoir conditions. For this reason, all samples aged in $scCO_2$–saturated brine are compared to those aged in N_2–saturated brine to evaluate relative effects of the former.

3.2 Microscopy, Spectroscopy, and X-ray Diffraction

Before and/or after aging in either $scCO_2$- or N_2-saturated brine, various tools were used to characterize selected samples. A microCT Scanner (X-TEK XT H 225 X-ray system) was used to characterize overall sample integrity and structure. The beam current was set at 185 μA, and the beam energy was set at 100 kV. The full core was imaged at a resolution of 120 μm, with selected samples imaged at 19 μm resolution. Subsets of the total sample were processed using the NIH-supported digital image processing software ImageJ, with a size of approximately 3x3x6 mm^3. Image processing was performed by applying Anisotropic Diffusion 2D filtering followed by statistical region merging (Q=25) to segment the image into separate pore spaces

and grains [46]–[48]. The porosity was obtained by viewing the histogram of the final segmented images.

A Leica DM 2500 compound light microscope with a Nikon camera was used in brightfield mode with an exposure time of 10 ms to image thin sections. A JEOL JSM-6490LV scanning electron microscope (SEM) coupled with energy dispersive spectroscopy (EDS) was used to identify changes in surface morphology, mineral grain exposure, and clay coatings. The samples were non-conductive, so SEM was used in low-vacuum mode. A Wyko NT 9100 Optical Profilometer was used to measure the surface roughness of each sample. The data was collected using a 5X lens with a 0.55x field of view and set to different scan ranges for each sample, from 40 μm to 360 μm, depending on the roughness of the surface. The roughness was calculated using Vision software.

X-ray diffraction (XRD) was used to characterize mineralogical composition. Approximately 1 g of each sample was ground to a fine powder with a mortar and pestle and passed through a 50-μm sieve before being sent to Premier Oilfield Laboratories for analysis. Brine analysis was performed with an ICP-Optical Emission Spectrometer (Varian 710-ES) before and after subsample aging to complement XRD results. Standard solutions for calibration were created using elements that comprise minerals expected to occur based on prior analyses of Mt. Simon sandstone material from a nearby depth interval, i.e., Al, Si, Ca, Fe, K, and Mg [43].

3.3 PHREEQC Modeling

A predictive geochemical model was run using the program PHREEQC to compare the experimentally observed brine composition to the theoretical final brine composition of the equilibrated system. The input minerals were based upon the mineralogy identified through XRD analysis. The model was run by first equilibrating the synthetic brine with the gas phase at

experimental pressure (22 MPa), then equilibrating that solution at experimental temperature (52°C), and finally equilibrating that solution with the minerals present in the Mt. Simon. The results of the model predict the final concentrations of all aqueous phase ions and solids in different possible mineral forms. For this study, only the aqueous phase ionic concentrations were necessary.

3.4 Geomechanical Methods

Fracture toughness was measured on samples before and after aging using a micro-scratch setup developed for reservoir rock analysis [34], [49] (Figure 1). The apparatus includes a moving stage, onto which the sample was clamped between two acrylic spacers in a stainless-steel vice. A diamond-tipped stylus with an equilibrium load was then lowered to contact the surface to create a height map to account for variations due to surface heterogeneity. Then, a 24.5 N constant load was applied. An Arduino-controlled motor moved the stage at constant velocity. Linear Variable Data Transformers (LVDT) recorded depth and horizontal displacement over each 5 mm scratch. The load cell recorded transverse force. Scratch tests were performed on dry subsamples as well as wet subsamples saturated with brine by submerging for 20 minutes to ensure entry into pore spaces. The latter was done to better represent clay plasticity in the Mt. Simon sample.

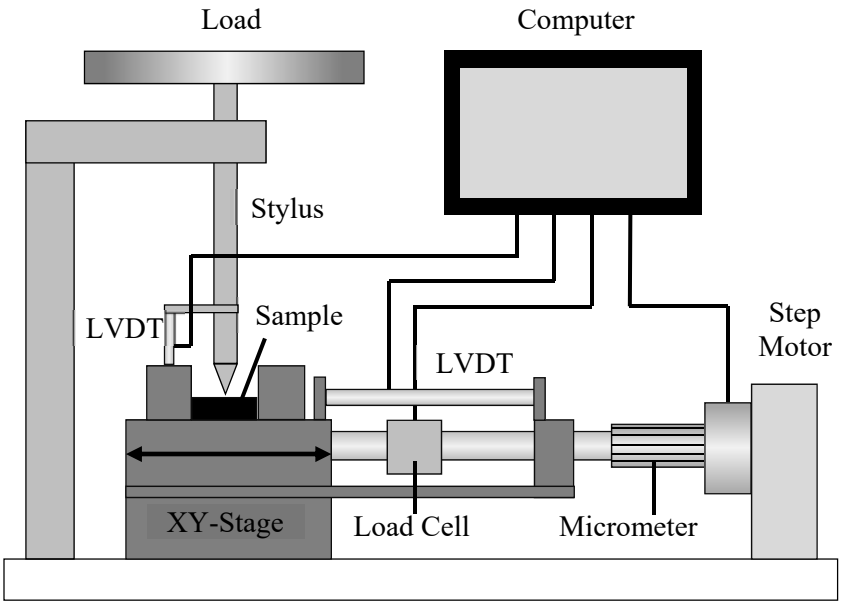

Figure 1: Geomechanical Micro-Scratch Test Apparatus.

All data, along with constant load, was used to calculate fracture toughness (K_c) through Equation 1 [49]:

$$K_c = \frac{F_T}{\sqrt{2pA}} \quad [\text{MPa m}^{1/2}] \qquad \text{Equation 1}$$

For this equation, F_T is horizontal force, and $2pA$ is a shape function for the conical diamond stylus. For this stylus, p is the total perimeter of the cone and A is the area of the stylus tip scratching the rock. Scratch depth is measured and used with the known geometric dimensions of the stylus (120° cone) to give the shape function along the entirety of the scratch. The average fracture toughness over the 5 mm scratch is the final output value with all tests averaged for final values.

4. Results

4.1 Sample heterogeneity

A cross-sectional micro-CT scan of the initial 2111.35 m (6927 ft) core is shown in Figure 2, along with a brightfield image of a vertical thin section from the same sample. Darker areas correspond to increased porosity, which occurs in horizontal planes. Heterogeneity is evident from both images, with variation in grain size and porosity that make apparent bedding planes. The largest and most porous layer has a 2D porosity of 6.67%, and the lowest and most compact layer has a 2D porosity of 0.03%

The thin section identified mineralogical heterogeneity and cementation. Large, translucent grains are quartz, and those with mottled surfaces are feldspar. Cementing these together is red-brown fibrous material, characteristic of clays with embedded iron. These observations are confirmed by SEM imaging and EDS elemental confirmation, matching expected mineralogical composition of illite and illite-smectite present in the Mt. Simon (Figure S1). The clays appear to be the fundamental structural component that determines sample integrity. The same clay cementation regime was observed in the Mt. Simon sandstone material from depth 2129.25 m (6985.72 ft) [44] and the entire Middle Mt. Simon [43].

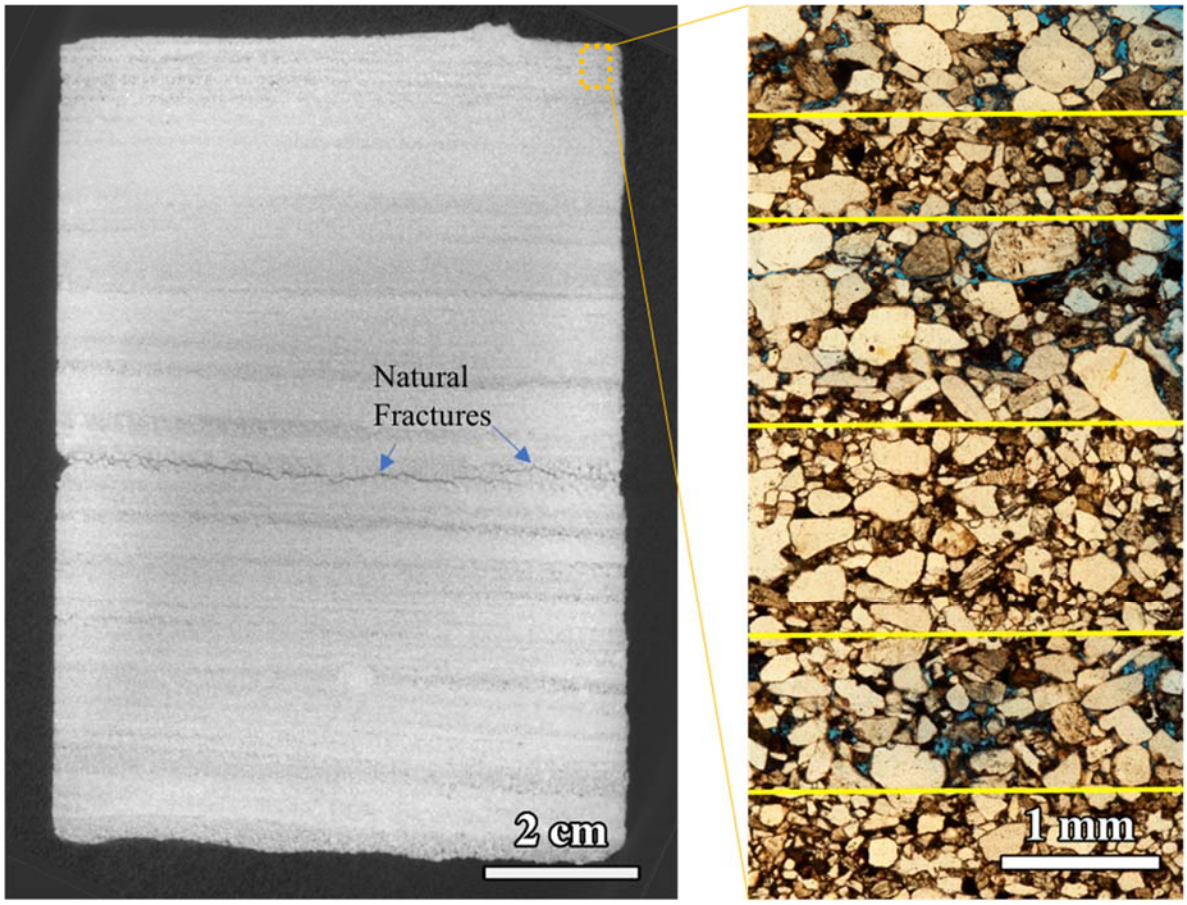

Figure 2: (a) MicroCT cross-sectional image showing heterogeneous bedding planes of the Mt. Simon 2111.35 m (6927 ft) core and (b) a vertical thin section from the top of the core. Yellow lines approximate the limits of bedding planes. The 2-dimensional porosities of the middle four layers are 2.95%, 6.67%, 0.03%, and 5.07% from top to bottom.

4.2 Changes in Sample Structure with Aging

CT scans (19 μm resolution) were taken of an unaged sample (MS2), and of subsamples aged 8 weeks in either N_2- (MS4) or scCO_2-saturated brine (MS2); representative side-view images are shown in Figure 3. The unaged sample (Figure 3a) exhibits the characteristic bedding planes seen previously in Figure 2. After aging for 8 weeks at reservoir conditions in N_2-saturated brine, the sample (MS4) shows signs of integrity degradation, with microfractures along the coarse bedding planes appearing at several locations (Figure 3b). Along one significant fracture, the MS4 sample separated into two pieces during handling when the sample had been

277 dried and removed from the reactor. The sample aged in $scCO_2$–saturated brine (MS2) also
278 shows signs of integrity degradation, but to a much greater extent (Figure 3c). Microfractures
279 propagated along both coarse and fine horizontal bedding planes. This weakening resulted in
280 sections of the sample falling away inside the pressure vessel, resulting in an altered overall
281 geometry, as well as opened bedding planes (Figure 3c). Due to sample fragility, MS2 was not
282 washed after 8 weeks of aging, and precipitated small NaCl and KCl salt crystals. The significant
283 structural changes are due in part to depressurization, and the greater fracturing in MS2 versus
284 MS4 could have been exacerbated by the higher solubility of $scCO_2$ than N_2 [50]. The sapphire
285 windows of the reactor allowed for viewing of the sample before depressurization; multiple
286 hairline fractures were observed in MS2, as well as in the replicate $scCO_2$-aged sample, MS1,
287 while only one hairline fracture was observed in MS4. Therefore, more extensive sample
288 fracturing in MS2 versus MS4 appears to be due in part to more extensive reaction with $scCO_2$
289 versus N_2, with fracturing exacerbated by depressurization.

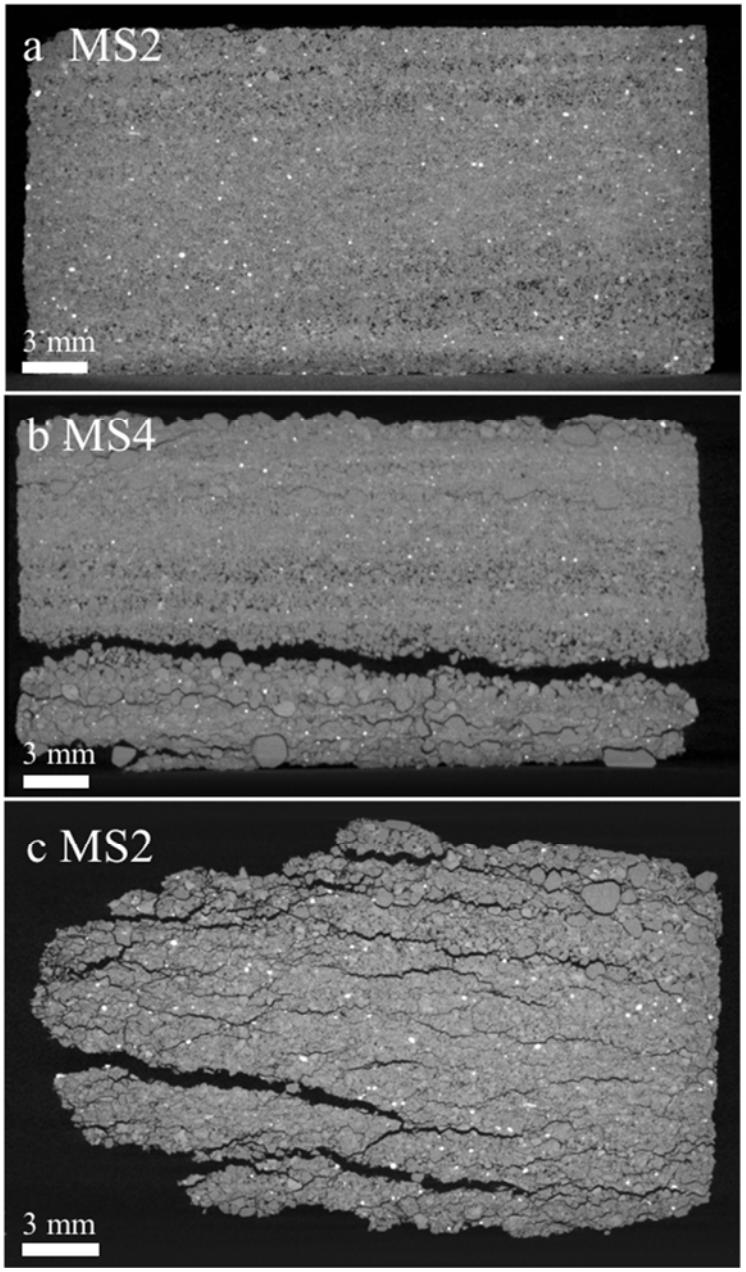

Figure 3: CT Scans of 2111.35 m (6927 ft) samples before and after experimentation. (a) Sample MS2, initial, (b) Sample MS4 after 8 weeks N_2 exposure, and (c) Sample MS2, 8 weeks exposure to scCO_2-saturated brine.

Changes in porosity before and after aging were determined from the CT scans analyzed by ImageJ functions. A 1 cm^3 section was selected within the MS2 sample, where the material had not opened along large fractures; corresponding images are compared in Figure S3. After prolonged contact with scCO_2-saturated brine, the calculated porosity values increased from

299 8.1% (unaged) to 15.8%. The value of 8.1% is similar to prior values determined for the Mt.
300 Simon sandstone, which range from 3-15% in the 6000-7000ft region measured through
301 petrographic image analysis of thin sections spanning the entire Mt. Simon formation [51]. The
302 same size specimen was selected for the MS4 sample. After prolonged contact with the N_2-
303 saturated brine, the calculated porosity was 9.6%. There was no initial CT scan made to
304 compare, but the sample aged in N_2-saturated brine came from a horizontally adjacent location to
305 MS2 on the 6-in long core for easy comparison. The porosity increase upon exposure to $scCO_2$–
306 saturated brine is consistent with other studies measured by petrographic studies [52] and micro-
307 CT scans [35].
308 To determine the source of the increase in void space (i.e., small effects by dissolution vs.
309 larger open fractures), a connectivity analysis was performed of the three-dimensional pore
310 structure through ImageJ. The connectivity analysis plugin identifies clusters of voxels within an
311 image based upon selected criteria, e.g., intensity values of pixels corresponding to pores or
312 grains in a segmented image. This is a way of analyzing the volumes of individual pores that
313 make up the porosity. The connected regions between the initial and final result showed similar
314 profiles, with some change at the extreme size range of pore volume (Figure S2). The smallest
315 pore space at this resolution was a 19x19x19 μm^3 voxel, or 6859 μm^3 or 6.9E-6 μL. After aging,
316 the MS2 sample had a 40% decrease in the total number of smallest pore spaces ranging in size
317 from 6.9E-6 μL - 5.5E-4 μL. There was a corresponding increase by 16% of the total number of
318 medium-sized connected regions of size 1.4E-3 μL – 6.9E-3 μL. These small volumetric changes
319 correspond to clay alterations around the grains (further discussed in SEM analysis). Larger
320 sections of connected pore spaces remained approximately equal after aging. The only
321 substantive change was two microfractures, measured as two large connected regions of 3.4 μL,

322 which were not present in the initial sample. These two fractures are a result of built up internal
323 stress allowing for a microfracture along coarse bedding planes in the Mt. Simon. The
324 connectivity analysis indicates that porosity increase after aging was due to both widening pore
325 spaces and the propagation of microfractures.

326 Low- and high-resolution SEM images of the same location on samples before and after
327 aging for 4 or 8 weeks in either N_2- or $scCO_2$-saturated brine were collected. Results for sample
328 MS3 before and after aging in N_2-saturated brine for 4 weeks are shown in Figure 4. Grains are
329 visible within the matrix of cementitious clays. Comparison of the low-resolution SEM images
330 (Figure 3a,c) before and after aging indicates no change in the sample surface structure. Some
331 salt precipitates are visible after aging. The high-resolution SEM images (Figure 3b,d) show the
332 fibrous illite-smectite clay sheets adhering to the grains with no apparent change in the sample
333 surface structure after aging. Images for the replicate subsample (MS4) show similar trends
334 (Figure S4).

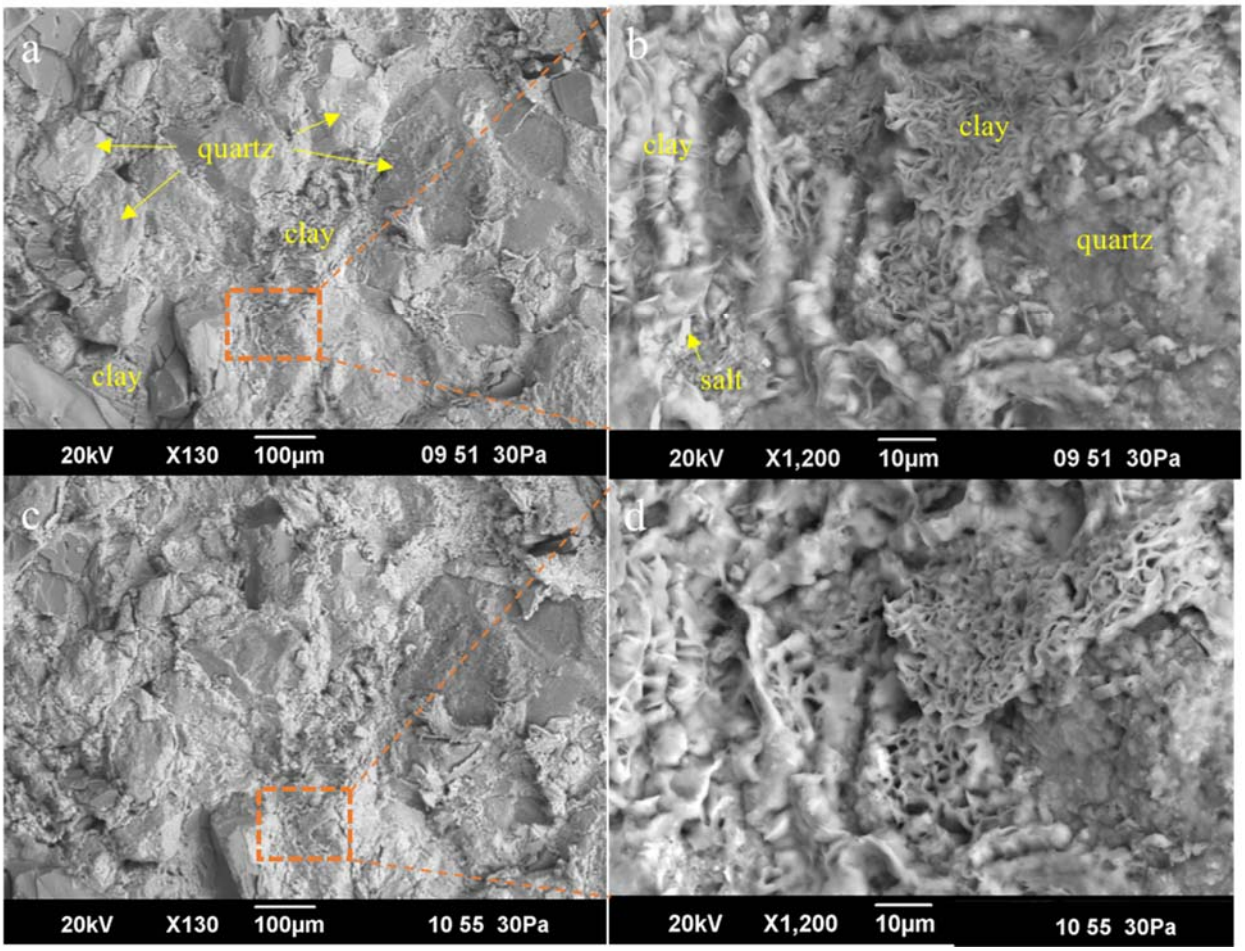

Figure 4: SEM images of MS3 (a,b) initial sample and (c,d) sample aged 4 weeks in N_2. The orange boxes in (a) and (c) are enlarged to examine the illite-smectite clay structure in (b) and (d), which appear structurally unchanged after exposure.

Low- and high-resolution SEM images of the same location on the MS1 sample before and after 4-weeks of aging in scCO_2-saturated brine are shown in Figure 5. SEM images of the corresponding MS2 subsample before and after 4 and 8-weeks of aging are presented in the SI and show similar results (Figure S5). The lower resolution SEM images (Figure 5a,c) indicate that after 4 weeks of aging, the clay matrix begins to disconnect from grain surfaces at some locations. After 8 weeks (Figure 5e), the clay matrix disconnects from grains at additional locations, and a large quartz grain is lost from the sample entirely, likely due to loss of cementation and the ethanol wash. High-resolution SEM images (5b,d,f) indicate alteration of

the clay matrix. At some locations, the fibrous illite-smectite clay sheets appear more separated and porous, and at others some clay appears to have been lost. Yellow arrows within 5(c,d,e) highlight specific points of lost clay contact.

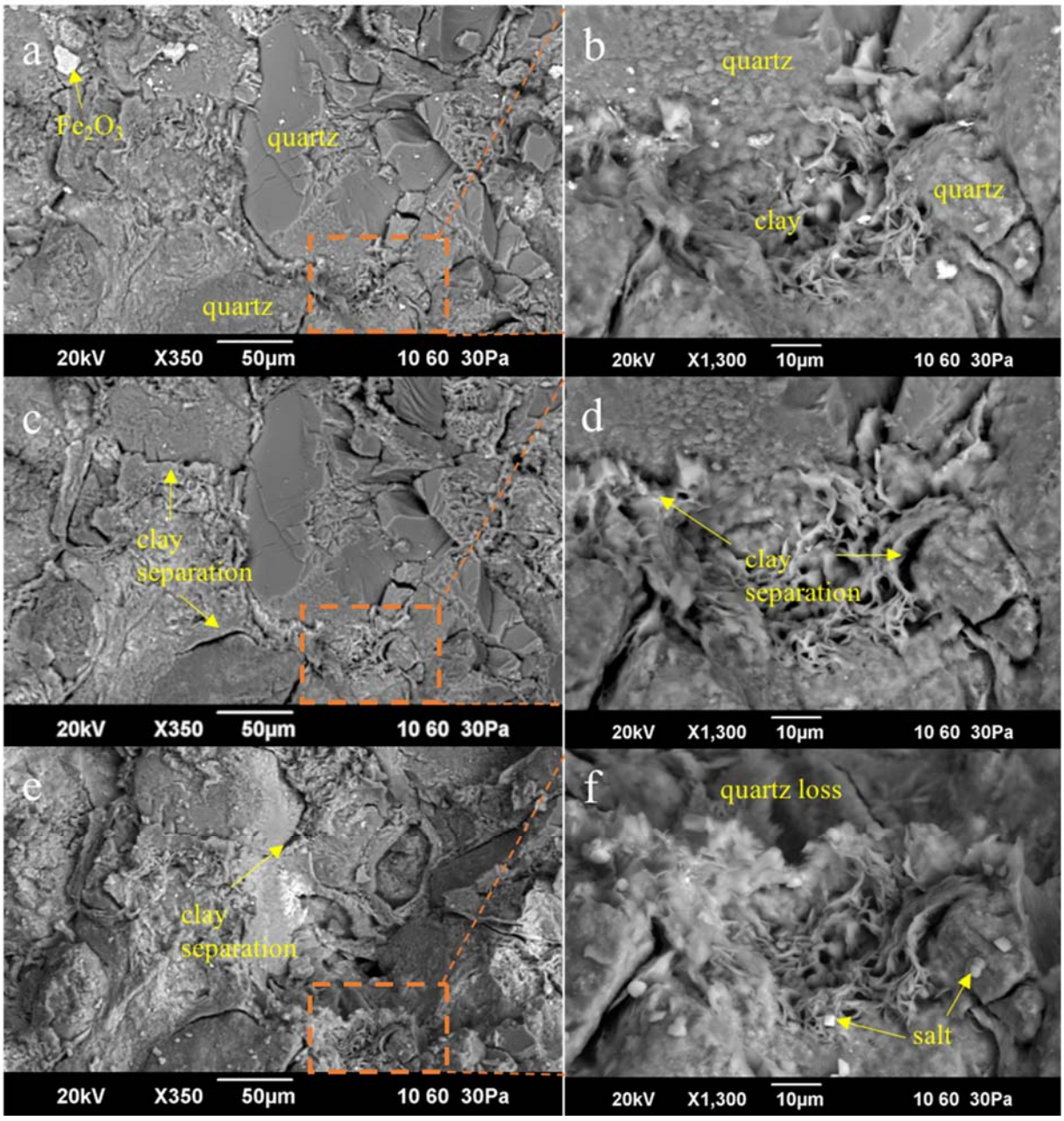

Figure 5: SEM images of MS1 (a,b) initial, (c,d) 4-week, and (e,f) 8-week samples aged in CO_2 with significant changes in structure. The orange square boxes in (a), (c), and (e) highlight the region of high-resolution imagery in (b), (d), and (f). Over increasing contact, clays separate from quartz grains to the point of quartz loss.

Overall, significantly more alteration of the cementing clay matrix at grain surfaces is evident in the sample aged in $scCO_2$-saturated brine compared to the sample aged in N_2-saturated brine. Both samples contain smectite clays, which swell when wetted. The impacts of swelling could be exacerbated by dissolution in the low pH conditions of the $scCO_2$-saturated brine system to create further separation of the clays and grain at points of contact. This work determines that reaction with $scCO_2$-saturated brine leads to clay detachment, possibly from a combination of mechanisms, including loss of clay by dissolution, weathering reactions, and swelling-drying effects. Our results are the first to explicitly show clay detachment from grain surfaces after aging in $scCO_2$-saturated brine.

Surface roughness results for samples aged in N_2 or $scCO_2$-saturated brine are presented in Figure 6, along with surface profilometry results from a representative section of MS1. The field of view is 0.95 mm by 1.3 mm, and the resolution is 1.98 μm. A comparative surface profile is shown in Figure 6a and 6b for subsample MS1, showing deepening of pits and limited precipitation of salt. Roughness parameters determined from five averaged surface profiles of either the MS1 or MS4 subsamples are in Figure 6c. The mean roughness of the N_2-aged samples increases from 30.9 μm to 30.97 μm and then 36.8 μm from the initial sample to 4 and then 8 weeks of exposure, respectively, but the increases are not significant with respect to the standard deviation. The mean roughness of the sample aged in $scCO_2$-saturated brine increases from 33.9 μm to 39.02 μm and then 55.4 μm for the same time periods, respectively, and the increase between 0 and 8 weeks is significant. This increase correlates to loss of grains and larger grain separations observed in the CT and SEM images.

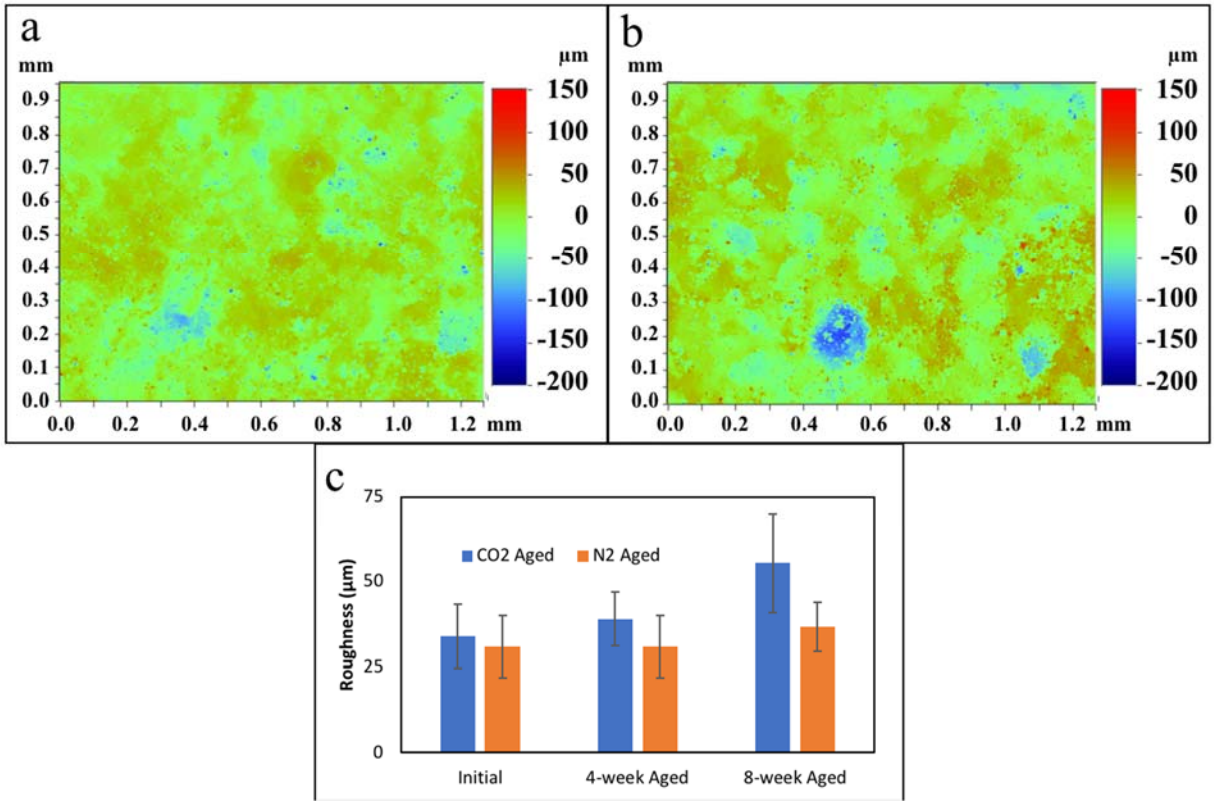

Figure 6: (a) Surface profile map of initial MS1 sample, (b) Surface profile map of 8-week aged MS1 sample, and (c) average roughness values for initial and aged CO_2 sample (MS1) and aged N_2 sample (MS4).

4.3 Changes in Mineralogy with Aging

XRD analysis was performed on samples before and after aging for 4-weeks in N_2- or CO_2-saturated brine to evaluate changes in mineralogy. Clay quantification values are known to a confidence of ±3%, with all other mineral confidence at ±1%. Results are shown in Table 2.

Table 2: XRD Mineralogical Data for initial, 8-week CO_2-aged sample (MS1) and 8-week N_2-aged sample (MS4). Tr indicates <0.5.

Mineral	**Formula**	**MS1 Initial % composition**	**MS4 (N_2) Aged % composition**	**MS1 (CO_2) Aged % composition**
Quartz	SiO_2	75.7	66.1	60.6
K-Feldspar	$KAlSi_3O_8$	17.0	20.4	25.0
Calcite	$CaCO_3$	0.8	1.2	1.1
Dolomite, Fe	$CaFe(CO_3)_2$	Tr	0.5	0.6
Illite	$(K,H_3O)(Al,Mg,Fe)_2$	2.8	5.0	5.4

	$(Si,Al)_4O_{10}[(OH)_2 \cdot n(H_2O)]$			
Illite/ smectite	$(Na,Ca)_{0.33}(Al,Mg)_2(Si_4O_{10})[(OH)_2 \cdot nH_2O]$	3.1	5.8	4.4
Hematite	Fe_2O_3	0.6	1.0	0.8
Halite	NaCl	Tr	Tr	2.1

389

390 The mineralogy of the Mt. Simon samples studied here correspond to the expected
391 mineralogy of the formation. The primary components are quartz and K-feldspar with minimal
392 carbonate. The relative percentage of quartz is less in the N_2 and CO_2-aged samples vs. the initial
393 materials. Since quartz is relatively nonreactive under the aging conditions after only 8 weeks,
394 the difference in quartz content is likely due to both sample hetereogeneity and the loss of
395 surface quartz grains from weakened cementation, leaving a surface dominated by K-feldspar
396 and the remaining clays. This observation is consistent with the surficial changes observed in the
397 SEM analyses (Figure 5). In terms of clays, the CO_2-aged sample has a higher ratio of illite to
398 illite/smectite clay (0.86 in MS4 vs. 1.22 in MS2). Smectites undergo illitization at high
399 pressures and temperatures under acidic conditions [18]. In both N_2 and CO_2-aged samples, the
400 relative percentage of clays increases to approximately equal total clays (i.e. 10%) when
401 considering the margin of error (±3%). Without significant changes between the N_2 and CO_2-
402 aged samples, there is no confirmation of clay dissolution due to pH. A general issue in the
403 analysis of Mt. Simon samples by XRD is heterogeneity inherent in the Mt. Simon sandstone,
404 exacerbated by the small sample size. Quantitative analysis of small volumes of clays in a
405 quartz-dominated sandstone is challenging, and the XRD results should be considered
406 qualitatively alongside the preceding methods of analyses. Therefore, the XRD results serve to
407 support the analyses of the SEM and micro-CT images showing the loss of cementation of grains
408 at contact points after aging in scCO_2-saturated brine, not the general dissolution of clays.

Fresh brine and brine collected from aged samples were analyzed by ICP-OES for Ca, K, Mg, Al, Fe, and Si as indicators of mineral reaction. These cationic concentrations are shown in Figure S6. Ultimately, the replicate samples exhibit variation on the same order of changes between the two conditions, and no direct trend could be confirmed. PHREEQC was used to model all ionic components present in solution after brine equilibration with the Mt. Simon sandstone and CO_2 or N_2 at experimental conditions (Figure S7). The final pH for the CO_2 system is 3.9, whereas the N_2 system is 5.9. In either case, the ionic concentrations found following experimentation determined that the system did not reach equilibrium in such a short experimental window.

4.4 Physical and Geomechanical Alteration

Scratch tests were performed on dry and wet samples to measure fracture toughness before and after exposure to both N_2 and $scCO_2$–saturated brine. Average fracture toughness values were determined from these results, which are shown in Figure 7 for all samples. For dry MS1 and MS2 subsamples aged in CO_2-saturated brine, the fracture toughness decreased significantly. The average decrease was 32.1% after four weeks and 69.5% after 8 weeks. In contrast, for dry MS3 and MS4 subsamples aged in N_2-saturated brine, the fracture toughness only decreased by 8.7% after 4 weeks and 16.9% after 8 weeks, within the standard deviation of the initial toughness. The results indicate that aging in $scCO_2$-saturated brine decreases sample strength more than aging in N_2-saturated brine.

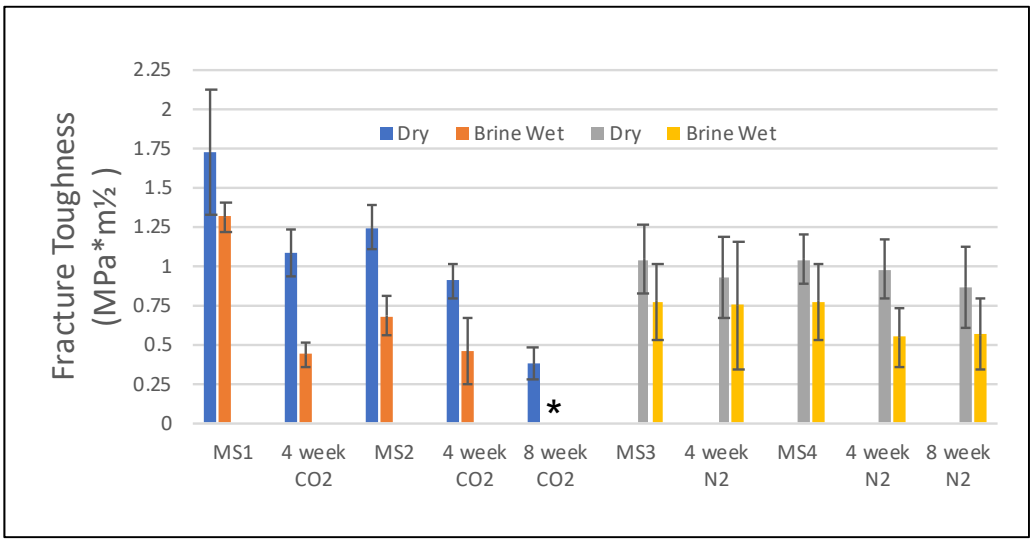

Figure 7: Scratch test results showing average fracture toughness of all samples. *In the case of MS2, the wetted 8-week CO_2 sample, when the stylus was weighted, the tip sank immediately through the sample with no resistance.

Scratch tests were conducted on wetted samples in order to examine the effect clay plasticity had on geomechanics. Comparisons are made to the respective dry measurement. For most initial samples, the wetted fracture toughness was 25% lower compared to the dry value, except for MS2, which was 45% lower. The values for wet scratch data tend to have higher variation. When examined as a trend in aging or in comparison to the dry fracture toughness, no statistically significant results can be drawn about geomechanical changes based solely on the wet scratch data.

5.0 Discussion

Subsamples were taken from a Mt. Simon sandstone core and aged in N_2 or scCO_2-saturated brine for 4 or 8 weeks at reservoir conditions. CT scans of these samples before and after aging indicate microfractures develop along coarser bedding planes during aging. At least some of these fractures likely developed due to internal pressure buildup induced by depressurization and cooling of the samples. However, we note that this effect is markedly more

pronounced under $scCO_2$-aging conditions, indicating the more acidic conditions created by $scCO_2$ lead to greater loss of integrity. The more acidic conditions also correspond to a greater increase in porosity. SEM images of these samples before and after aging indicate that cementitious clays, which appear to bind larger quartz and feldspar grains together, pull away from grain surfaces when aged in $scCO_2$-saturated brine, but not in N_2-saturated brine. This process appears to have contributed to the significant increase in surface roughness in CO_2-aged subsamples, which was not apparent in the N_2-aged subsample. This process also likely contributed to the greater number and extent of fractures observed by CT scanning in the CO_2-aged subsample.

Clay contact alternations may have also led to a decrease in clay coatings and an increase in porosity observed by others in the Mt. Simon sandstone, after subjecting it to $scCO_2$-saturated brine (20.7MPa, 50°C) for 6 months [18]. Outside of the Mt. Simon, previous experimental studies have observed significant dissolution and conversion of clays in geologic carbon sequestration laboratory experiments [5]. In our work, XRD results and brine cation analysis qualitatively indicate that large scale dissolution of clays did not occur on a short timescale (8 weeks), but that there was significant ionic exchange between the clays and brine of ions with greater affinity. From the structural and limited mineralogical changes, we conclude that the primary physical alteration occurred at the contact between cementing clays and silicate grains due to enhanced reaction in $scCO_2$-saturated brine.

Our work further connects geochemical changes to mechanical effects. Specifically, fracture toughness was measured before and after aging in N_2 or $scCO_2$-saturated brine. Large and significant changes were observed for dried samples aged in CO_2-saturated brine, but not for dry samples aged in N_2-satuated brine. These results are consistent with SEM results showing

471 clay detachment from grain surfaces for samples aged in CO_2-saturated brine, and no clay
472 detachment for samples aged in N_2-saturated brine. We note, however, that significant changes in
473 fracture toughness for wet samples were not apparent before and after aging events. This may be
474 due to the larger uncertainty associated with these measurements, and the overall lowering of
475 fracture toughness due to clay plasticity.

476 In similar work fracture toughness was measured before and after aging Entrada
477 sandstone and Summerville siltstone in neutral and $scCO_2$-saturated brine for 1-4 weeks at 9-10
478 MPa at 80°C [35]. That work measured decreases in fracture toughness higher than those
479 reported here, i.e., from 50-87% depending on time and experimental conditions, likely due to
480 the greater proportion of calcite and clays. As in this work, the Entrada sandstone was
481 particularly altered after exposure to $scCO_2$-saturated brine, exhibiting cracks and preferential
482 dissolution at the sample surface in both thin sections and micro CT imagery. Our results for the
483 Mt. Simon sandstone indicate that clay detachment from grain surfaces upon exposure to $scCO_2$-
484 saturated brine contributed to at least some of the fracture toughness reduction observed by those
485 authors [35].

486 The results in this work are limited to batch reactors and do not evaluate the impact of
487 flow, where preferential flow paths can develop in higher porosity or fractured zones of reservoir
488 materials and lead to reactions along these paths. While batch experiments allow exposure of
489 reservoir materials to high concentrations of $scCO_2$ (e.g., near the well-bore, along preferential
490 flow paths), they do not allow the continuous renewal of reservoir water during flow that carries
491 away dissolved ions. The weakening of the clay cementation observed in this work may
492 correspond to the weakening of sandstone along faults under stress and strain, potentially
493 resulting in the observed microseismic activity observed during and following CO_2 injection in

494 the Mt. Simon formation. However, more work under a wider range of conditions (e.g., flow) is
495 required for confirmation. Regardless, results from this work should be considered for modeling
496 full reservoirs in future sequestration work. Generally, coupled chemical and geomechanical
497 effects observed in this and other work will serve to increase the field of knowledge for safe
498 practices in geologic CO_2 sequestration.
499
500 **6.0 Conclusions**
501 The fracture toughness in samples aged in CO_2-saturated brine is significantly reduced.
502 The CT scans illustrate this weakening through increased micro-fracturing along bedding planes
503 and increases in porosity. The SEM results indicate the mechanism of this weakening is clay
504 detachment from quartz and feldspar grain surfaces. The precise causes of the clay detachment
505 are unknown, but likely results from a combination of the internal stresses associated with
506 swelling and drying clays, as well as dissolution reactions at the most reactive surfaces in the
507 sandstone at low pH. We recognize that some of the sample alteration observed in this work are
508 due to the cycling of pressure and temperature that samples are exposed to in the laboratory.
509 However, the differences between acidified ($scCO_2$-saturated) and neutral (N_2-saturated) brine
510 indicate the former have clear impacts on the sandstone.
511 These results have implications for integrity of storage reservoirs in the field. Fracture
512 toughness results suggest carbon storage reservoirs may undergo geomechanical weakening with
513 CO_2 injection which can lead to redistribution of stresses that are able to induce fracture slippage
514 and trigger microseismic events. However, in the field the Mt. Simon sandstone is subject to
515 overburden stress, which could serve as a stabilizing force that maintains clay-grain contacts.
516 Also, it is not clear if sample alteration would be limited to near the wellbore or occur further out

517 in the formation. It would depend on the buffering capacity of the reservoir, and the injection rate
518 of the CO_2. Further work is necessary under reservoir conditions to determine the coupled
519 geochemical and geomechanical effects of aging in scCO_2-saturated brine on reservoir integrity.
520

521 **Acknowledgements**

522 This work was supported as part of the Center for Geologic Storage of CO2, an Energy
523 Frontier Research Center funded by the U.S. Department of Energy, Office of Science, Basic
524 Energy Sciences under Award # DE-SC0C12504. Data for this project were provided, in part, by
525 work supported by the U.S. Department of Energy under award number DE-FC26-05NT42588
526 and the Illinois Department of Commerce and Economic Opportunity. This research was
527 supported in part by an appointment to the U.S. Department of Energy (DOE) Postgraduate
528 Research Program at the National Energy Technology Laboratory administered by the Oak
529 Ridge Institute for Science and Education. We thank Luis Hernandez-Uribe, who provided the
530 Matlab code used to analyze scratch test data and determine fracture toughness values. We
531 acknowledge the Chevron Digital Petrophysics Laboratory
532 https://faculty.engr.utexas.edu/espinoza/microct, where X-ray microfocus scanning was
533 performed.
534

References

[1] IPCC, *Climate Change 2014: Synthesis Report. Contribution of Working Groups I, II, and III to the Fifth Assessment Report of the Intergovernmental Panel on Climate Change*. Geneva, Switzerland: IPCC, 2014.

[2] J. Rutqvist, "The Geomechanics of CO2 Storage in Deep Sedimentary Formations," *Geotech. Geol. Eng.*, vol. 30, no. 3, pp. 525–551, Jun. 2012.

[3] M. D. Zoback and S. M. Gorelick, "Earthquake triggering and large-scale geologic storage of carbon dioxide.," *Proc. Natl. Acad. Sci. U. S. A.*, vol. 109, no. 26, pp. 10164–8, Jun. 2012.

[4] I. Czernichowski-Lauriol, C. Rochelle, I. Gaus, M. Azaroual, J. Pearce, and P. Durst, "Geochemical interactions between CO2, pore-waters and reservoir rocks," *NATO Sci. Ser. IV Earth Environ. Sci.*, vol. 65, pp. 157–174, 2006.

[5] M. Wigand, J. W. Carey, H. Schütt, E. Spangenberg, and J. Erzinger, "Geochemical effects of CO2 sequestration in sandstones under simulated in situ conditions of deep saline aquifers," *Appl. Geochemistry*, vol. 23, no. 9, pp. 2735–2745, 2008.

[6] H. Deng, J. P. Fitts, D. Crandall, D. McIntyre, and C. A. Peters, "Alterations of fractures in carbonate rocks by CO2-acidified brines," *Environ. Sci. Technol.*, vol. 49, no. 16, pp. 10226–10234, Aug. 2015.

[7] X. Wang, V. Alvarado, N. Swoboda-Colberg, and J. P. Kaszuba, "Reactivity of dolomite in water-saturated supercritical carbon dioxide: Significance for carbon capture and storage and for enhanced oil and gas recovery," *Energy Convers. Manag.*, vol. 65, pp. 564–573, 2013.

[8] M. Wigley, B. Dubacq, N. Kampman, and M. Bickle, "Controls of sluggish, CO2-promoted, hematite and K-feldspar dissolution kinetics in sandstones," *Earth Planet. Sci. Lett.*, vol. 362, pp. 76–87, 2013.

[9] J. Rosenqvist, A. D. Kilpatrick, B. W. D. Yardley, and C. A. Rochelle, "Feldspar dissolution at CO2-saturated conditions," in *EGU General Assembly*, 2014.

[10] K. Amram and J. Ganor, "The combined effect of pH and temperature on smectite dissolution rate under acidic conditions," *Geochim. Cosmochim. Acta*, vol. 69, no. 10, pp. 2535–2546, 2005.

[11] V. N. Balashov, G. D. Guthrie, J. A. Hakala, C. L. Lopano, J. D. Rimstidt, and S. L. Brantley, "Predictive modeling of CO2 sequestration in deep saline sandstone reservoirs: Impacts of geochemical kinetics," *Appl. Geochemistry*, vol. 30, pp. 41–56, Mar. 2013.

[12] T. Xu, J. A. Apps, and K. Pruess, "Mineral sequestration of carbon dioxide in a sandstone-shale system," *Chem. Geol.*, vol. 217, pp. 295–318, 2005.

[13] P. Audigane, I. Gaus, I. Czernichowski-Lauriol, K. Pruess, and T. Xu, "Two-dimensional reactive transport modeling of CO2 injection in a saline aquifer at the Sleipner site, North Sea," *Am. J. Sci.*, vol. 307, no. 7, pp. 974–1008, Sep. 2007.

[14] J. Rohmer, A. Pluymakers, and F. Renard, "Mechano-chemical interactions in sedimentary rocks in the context of CO2 storage: Weak acid, weak effects?," *Earth Sci. Rev.*, vol. 157, pp. 86–110, 2016.

[15] T. Xu, J. A. Apps, and K. Pruess, "Reactive geochemical transport simulation to study mineral trapping for CO2 disposal in deep arenaceous formations," *J. Geophys. Res. Solid Earth*, vol. 108, no. B2, Feb. 2003.

[16] S. Hangx, A. van der Linden, F. Marcelis, and A. Bauer, "The effect of CO2 on the

mechanical properties of the Captain Sandstone: Geological storage of CO2 at the Goldeneye field (UK)," *Int. J. Greenh. Gas Control*, vol. 19, pp. 609–619, Nov. 2013.

[17] O. Walderhaug, "Kinetic Modeling of Quartz Cementation and Porosity Loss in Deeply Buried Sandstone Reservoirs," *Am. Assoc. Pet. Geol. Bull.*, vol. 80, no. 5, pp. 731–745, 1996.

[18] L. E. Yoksoulian, J. T. Freiburg, S. K. Butler, P. M. Berger, and W. R. Roy, "Mineralogical alterations during laboratory-scale carbon sequestration experiments for the Illinois Basin," *Energy Procedia*, vol. 37, no. 37, pp. 5601–5611, 2013.

[19] K. Zemke, A. Liebscher, and M. Wandrey, "Petrophysical analysis to investigate the effects of carbon dioxide storage in a subsurface saline aquifer at Ketzin, Germany (CO 2 SINK)," *Int. J. Greenh. Gas Control*, vol. 4, pp. 990–999, 2010.

[20] C. M. Cerda, "Mobilization of kaolinite fines in porous media," *Colloids and Surfaces*, vol. 27, no. 1–3, pp. 219–241, Oct. 1987.

[21] P. Egermann, E. Bemer, and B. Zinszner, "An experimental investigation of the rock properties evolution associated to different levels of CO2 injection like alteration processes," *Int. Symp. Soc. Core Anal.*, pp. 1–15, 2006.

[22] J. K. Pearce, A. Golab, G. K. W. Dawson, L. Knuefing, C. Goodwin, and S. D. Golding, "Mineralogical controls on porosity and water chemistry during O2-SO2-CO2 reaction of CO2 storage reservoir and cap-rock core," *Appl. Geochemistry*, vol. 75, pp. 152–168, Dec. 2016.

[23] Y. Shao, H., Ray, J., Jun, "Dissolution and Precipitation of Clay Minerals under Geologic CO 2 Sequestration Conditions: CO 2 -Brine-Phlogopite Interactions," *Environ. Sci. Technol.*, no. 44, pp. 5999–6005, 2010.

[24] T. Xu, J. A. Apps, and K. Pruess, "Mineral sequestration of carbon dioxide in a sandstone–shale system," *Chem. Geol.*, vol. 217, pp. 295–318, 2005.

[25] V. N. Balashov, G. D. Guthrie, C. L. Lopano, J. A. Hakala, and S. L. Brantley, "Reaction and diffusion at the reservoir/shale interface during CO2 storage: Impact of geochemical kinetics," *Appl. Geochemistry*, vol. 61, pp. 119–131, Oct. 2015.

[26] Y. Mehmani, T. Sun, M. T. Balhoff, P. Eichhubl, and S. Bryant, "Multiblock Pore-Scale Modeling and Upscaling of Reactive Transport: Application to Carbon Sequestration," *Transp. Porous Media*, vol. 95, no. 2, pp. 305–326, Nov. 2012.

[27] J. M. Matter and P. B. Kelemen, "Permanent storage of carbon dioxide in geological reservoirs by mineral carbonation," *Nat. Geosci.*, vol. 2, no. 12, pp. 837–841, Dec. 2009.

[28] R. Shukla, P. Ranjith, A. Haque, and X. Choi, "A review of studies on CO 2 sequestration and caprock integrity," 2010.

[29] G. K. W. Dawson *et al.*, "ANLEC Project 3-1110-0101: Review of laboratory-scale geochemical and geomechanical experiments simulating geosequestration of CO2 in sandstone, and associated modelling studies," *Aust. Natl. Low Emiss. Coal Res. Dev. Manuka, ACT*, 2013.

[30] A. G. Ilgen, P. Newell, T. Hueckel, D. N. Espinoza, and M. Hu, *Coupled Chemical-Mechanical Processes Associated With the Injection of CO2 into Subsurface*. Elsevier, 2019.

[31] M. Iding and P. Ringrose, "Evaluating the impact of fractures on the performance of the In Salah CO2 storage site," *Int. J. Greenh. Gas Control*, vol. 4, no. 2, pp. 242–248, Mar. 2010.

[32] J. E. Streit and R. R. Hillis, "Estimating fault stability and sustainable fluid pressures for

underground storage of CO2 in porous rock," *Energy*, vol. 29, no. 9–10, pp. 1445–1456, Jul. 2004.

[33] C. D. Hawkes, P. J. McLellan, and S. Bachu, "Geomechanical Factors Affecting Geological Storage of CO2 in Depleted Oil and Gas Reservoirs," *J. Can. Pet. Technol.*, vol. 44, no. 10, Oct. 2005.

[34] Y. Sun, M. Aman, and D. N. Espinoza, "Assessment of mechanical rock alteration caused by CO2–water mixtures using indentation and scratch experiments," *Int. J. Greenh. Gas Control*, vol. 45, pp. 9–17, 2016.

[35] M. Aman, D. N. Espinoza, A. G. Ilgen, J. R. Major, P. Eichhubl, and T. A. Dewers, "CO2-induced chemo-mechanical alteration in reservoir rocks assessed via batch reaction experiments and scratch testing," *Greenh. Gases Sci. Technol.*, vol. 8, no. 1, pp. 133–149, Feb. 2018.

[36] D. N. Espinoza *et al.*, "CO2 charged brines changed rock strength and stiffness at Crystal Geyser, Utah: Implications for leaking subsurface CO2 storage reservoirs," *Int. J. Greenh. Gas Control*, vol. 73, pp. 16–28, Jun. 2018.

[37] A. G. Ilgen *et al.*, "Shale-brine-CO2 interactions and the long-term stability of carbonate-rich shale caprock," *Int. J. Greenh. Gas Control*, vol. 78, pp. 244–253, Nov. 2018.

[38] H. Marbler, K. P. Erickson, M. Schmidt, C. Lempp, and H. Pöllmann, "Geomechanical and geochemical effects on sandstones caused by the reaction with supercritical CO2: an experimental approach to in situ conditions in deep geological reservoirs," *Environ. Earth Sci.*, vol. 69, no. 6, pp. 1981–1998, Jul. 2013.

[39] J. O. Kaven, S. H. Hickman, A. F. Mcgarr, and W. L. Ellsworth, "Surface Monitoring of Microseismicity at the Decatur, Illinois, CO2 Sequestration Demonstration Site," *Seismol. Res. Lett.*, vol. 86, no. 4, 2015.

[40] B. P. Goertz-Allmann, S. J. Gibbons, V. Oye, R. Bauer, and R. Will, "Characterization of induced seismicity patterns derived from internal structure in event clusters," *J. Geophys. Res. Solid Earth*, vol. 122, no. 5, pp. 3875–3894, May 2017.

[41] R. Will, V. Smith, H. E. Leetaru, J. T. Freiburg, and D. W. Lee, "Microseismic Monitoring, Event Occurrence, and the Relationship to Subsurface Geology," *Energy Procedia*, vol. 63, pp. 4424–4436, 2014.

[42] R. A. Bauer, M. Carney, and R. J. Finley, "Overview of microseismic response to CO2 injection into the Mt. Simon saline reservoir at the Illinois Basin-Decatur Project," *Int. J. Greenh. Gas Control*, vol. 54, no. 1, pp. 378–388, 2016.

[43] J. T. Freiburg, D. G. Morse, H. E. Leetaru, R. P. Hoss, and Q. Yan, "A Depositional and Diagenetic Characterization of the Mt. Simon Sandstone at the Illinois Basin - Decatur Project Carbon Capture and Storage Site, Decatur, Illinois, USA," *Illinois State Geol. Surv. Prairie Res. Inst.*, 2014.

[44] J. Botto *et al.*, "Effects of Mineral Surface Properties on Supercritical CO2 Wettability in a Siliciclastic Reservoir," *Energy & Fuels*, p. acs.energyfuels.6b03336, 2017.

[45] O. Senel and N. Chugunov, "CO2 Injection in a Saline Formation: Pre-Injection Reservoir Modeling and Uncertainty Analysis for Illinois Basin – Decatur Project," *Energy Procedia*, vol. 37, pp. 4598–4611, 2013.

[46] V. Piling, J. Janacek, and J. Schindelin, "Anisotropic Diffusion 2D - ImageJ." [Online]. Available: http://www.ncbi.nlm.nih.gov/pubmed/15794157. [Accessed: 05-Jun-2019].

[47] J. Schindelin, "Statistical Region Merging - ImageJ." [Online]. Available: https://imagej.net/Statistical_Region_Merging. [Accessed: 05-Jun-2019].

[48] R. Nock and F. Nielsen, “Statistical region merging,” *IEEE Trans. Pattern Anal. Mach. Intell.*, vol. 26, no. 11, pp. 1452–1458, Nov. 2004.
[49] A.-T. Akono and F.-J. Ulm, “Fracture scaling relations for scratch tests of axisymmetric shape,” *J. Mech. Phys. Solids*, vol. 60, no. 3, pp. 379–390, Mar. 2012.
[50] Engineering ToolBox, “Solubility of Gases in Water,” 2008. [Online]. Available: https://www.engineeringtoolbox.com/gases-solubility-water-d_1148.html. [Accessed: 04-Jun-2019].
[51] B. B. Bowen *et al.*, “Depositional and diagenetic variability within the Cambrian Mount Simon Sandstone: Implications for carbon dioxide sequestration,” *Environ. Geosci.*, vol. 18, no. 2, pp. 69–89, 2011.
[52] J. Canal, J. Delgado, I. Falcón, Q. Yang, R. Juncosa, and V. Barrientos, “Injection of CO2-Saturated Water through a Siliceous Sandstone Plug from the Hontomin Test Site (Spain): Experiment and Modeling,” *Environ. Sci. Technol.*, vol. 47, no. 1, pp. 159–167, Jan. 2013.

SUPPORTING INFORMATION

Geochemical and geomechanical alteration of siliciclastic reservoir rock by supercritical CO_2-saturated brine formed during geological carbon sequestration

Samantha J. Fuchs[1], D. Nicholas Espinoza[2], Christina L. Lopano[3], C., Ange-Therese Akono[4], and Charles J. Werth[1*]

1. Department of Civil, Architecture and Environmental Engineering, University of Texas at Austin, 301 East Dean Keeton St., Austin, TX 78721
2. Department of Petroleum and Geosystems Engineering, University of Texas at Austin, 200 E Dean Keeton St., TX 78721
3. Office of Research and Development, US DOE - National Energy Technology Laboratory, 626 Cochrans Mill Road, P.O. Box 10940, Pittsburgh, PA 15236
4. Department of Civil and Environmental Engineering, Northwestern University, 2145 Sheridan Road, Evanston, IL 60208

* Corresponding Author: werth@utexas.edu, 217-377-6063

Supporting Information

The initial composition of synthetic brine used in the aging experiments is shown in Table S1 based upon previous synthetic brine recipes for the Mt. Simon [1].

Table S1: IDBP-G2017 Average Brine concentrations for the Mt. Simon Formation

Reagent	Mass (g/L)	Molecular Weight (mol/g)	Molarity (mol/L, M)
NaCl	111.6662	58.4	1.911
$CaCl_2 \cdot 2H_2O$	78.3458	147.0	0.533
KBr	6.48	119.0	0.054
Na_2SO_4	0.4820	142.0	0.003
$SrCl_2 \cdot 6H_2O$	2.3689	266.6	0.009
LiCl	9.3635	42.4	0.221

SEM-EDS was performed on a thin section of the Mt. Simon at a depth of 6927 ft. The observed elemental composition was related to the molecular formulas of quartz, K-feldspar, and clays expected by XRD analysis from the literature. K-feldspar, $KAlSi_3O_8$, was assigned to grains with K and Al percentages within 2% of each other. Clays were assigned based upon Al percentage being approximate two times higher that K. Illite-smectite contains numerous substitutions and ranges from 2-6% Fe content, higher than standard illite at 1.8% composition [2], due to the presence of iron oxides.

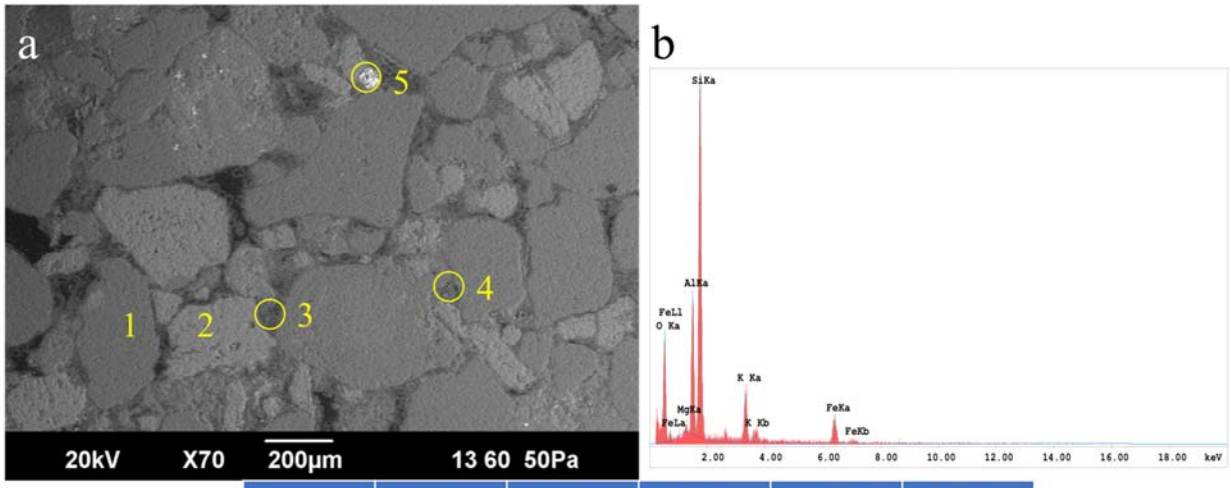

c	Site 1	Site 2	Site 3	Site 4	Site 5
	At%	At%	At%	A%	At%
O	36.66	41.04	41.85	40.83	42.00
Mg	-	-	1.02	0.62	-
Al	2.88	10.55	12.08	11.93	3.82
Si	57.93	38.37	37.46	36.56	27.34
K	1.94	9.75	5.34	5.04	1.52
Fe	0.59	0.29	2.25	5.02	23.91
Ti	-	-	-	-	1.40
	Quartz	K-feldspar	Illite	Illite-smectite	FeO_2 on quartz

Figure S1: (a) SEM image of thin section with highlighted points of analysis. (b) EDS spectra of Site 4 showing elemental peaks. (c) Table of composition by atomic percentage at each site, matched to mineralogy.

The volume of connected voxels in a subsection of the CT-image of sample MS2 was computed using ImageJ connectivity analysis. The results are shown in Figure S2 at normal and logarithmic scale.

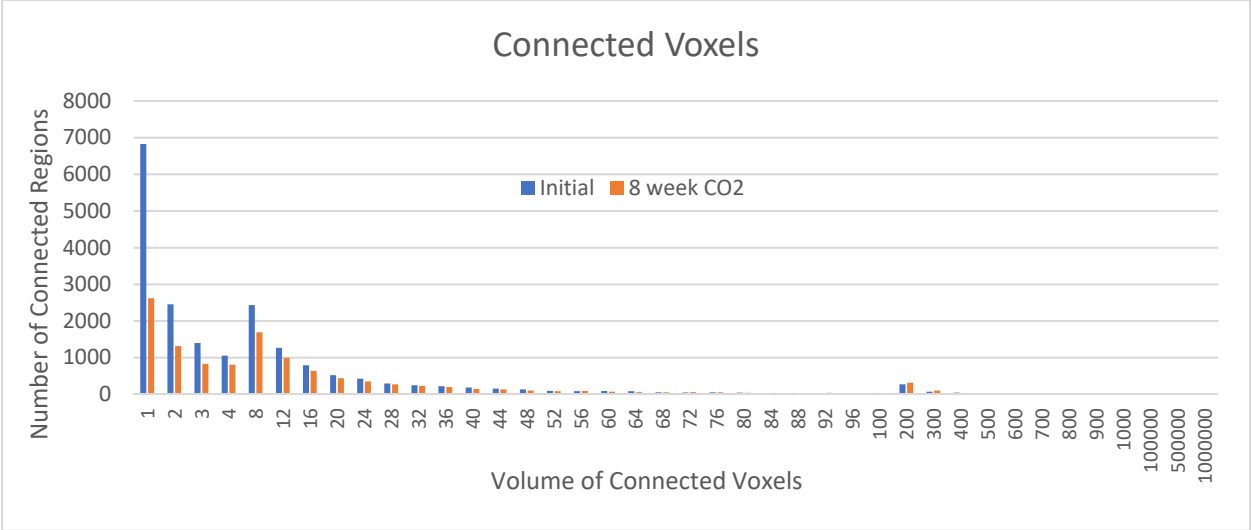

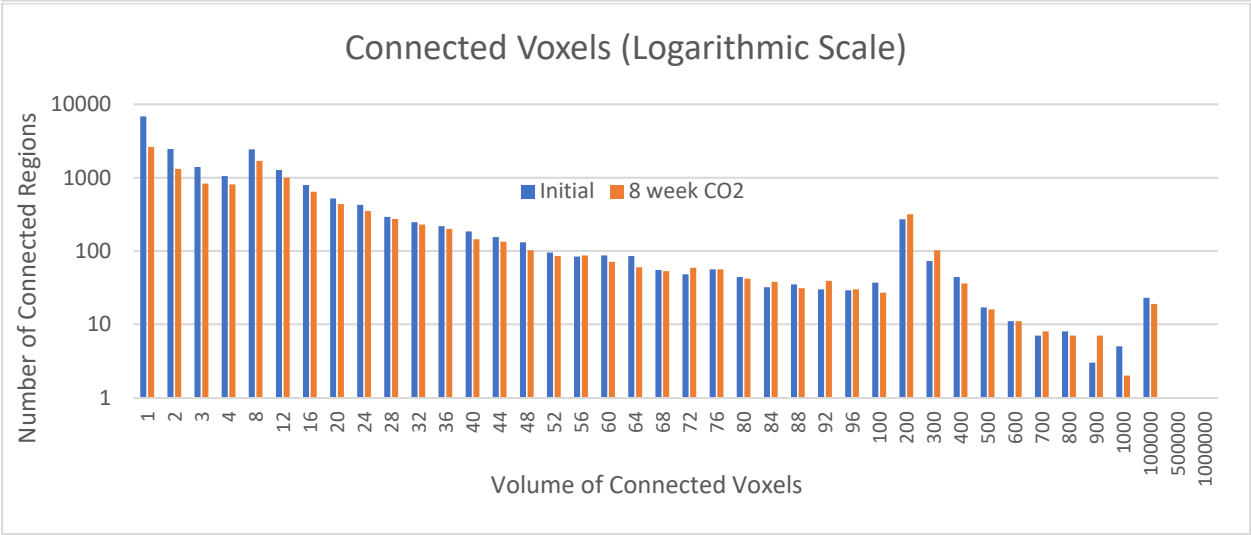

Figure S2: Connectivity of pore space in MS2 before and after 8 weeks exposure to $scCO_2$-saturated brine. Analysis shows smaller pore spaces expand in volume but do not form significant fracture networks. The two charts are the same, but with the second on a logarithmic scale to observe the tends towards increasingly larger connect volumes in the 72-900 range.

Figure S3 shows a subsection of the full CT scan of sample MS2. The sample was cropped to a 3x3x3cm cube, filtered with the ImageJ plugin Anisotropic Diffusion 2D, and then segmented with statistical region merging (Q=50) to identify pore space. Statistical region merging is a region growing and merging algorithm. It groups together voxels based upon their related values depending on the number of groups selected. The plugin write-up can be found at <https://imagej.net/Statistical_Region_Merging>. After segmentation, the porosity values of the

subsections were found to be 8.1% and 15.8% respectively. The same process was done for MS4, the N_2-saturated brine, and the subsection had a calculated porosity of 9.6%. The initial porosity measurements match previous analysis of the Mt. Simon formation for the 6000-7000ft range, ranging from 3-15% through both laboratory measurements and digital calculations [3].

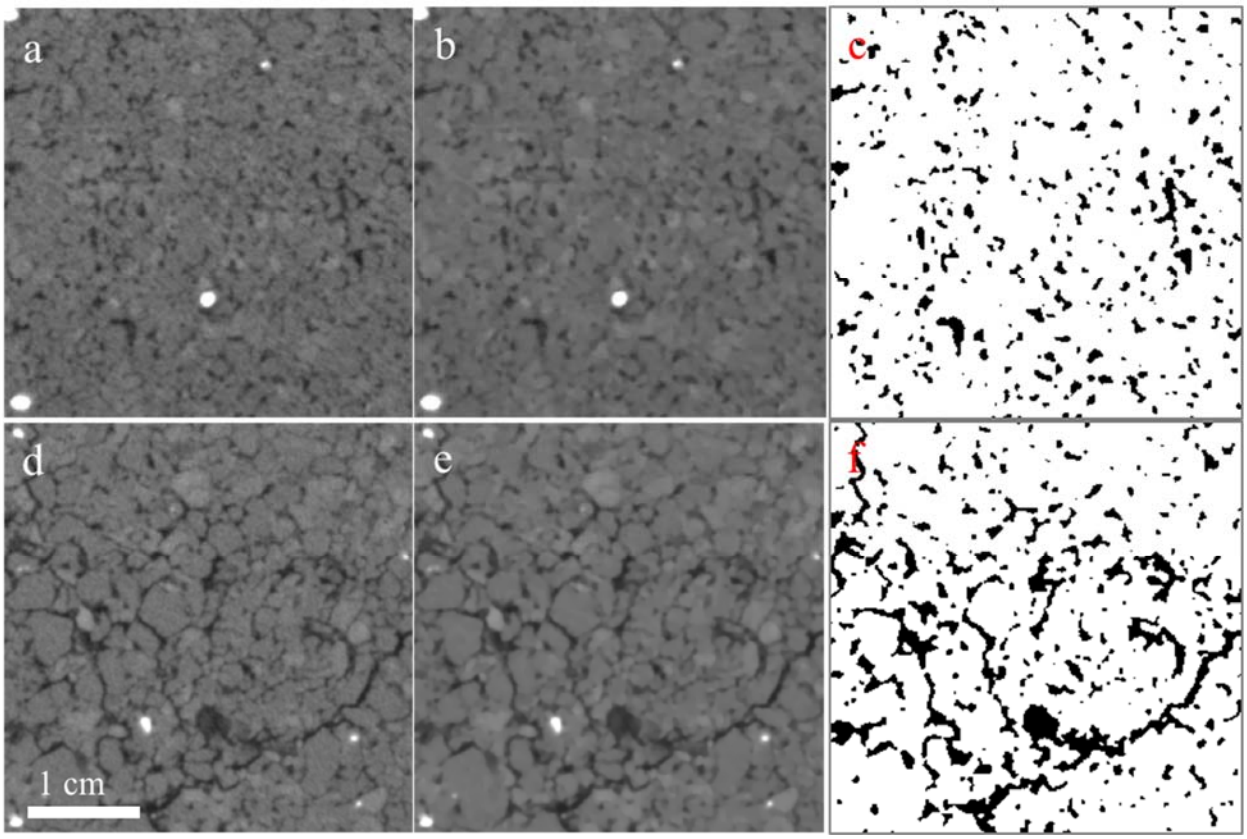

Figure S3: Subsections of the CT scan of Mt. Simon sample MS2 (a,b,c) before and (d,e,f) after 8 weeks exposure to $scCO_2$ saturated brine. Images (a) and (d) correspond to the initial CT scans. Images (b) and (e) show the subsample after Anisotropic Diffusion processing and images (d) and (f) show the final segmentation of the images.

Figure S4 shows the SEM images for the replicate N_2-saturated brine sample. After the first four weeks, there is insignificant change in the clay-grain structure, but after 8 weeks, the boundary of the largest quartz grain is disturbed, with multiple grains missing and clays separated. The clay coating over the grains in the center of the image are still present.

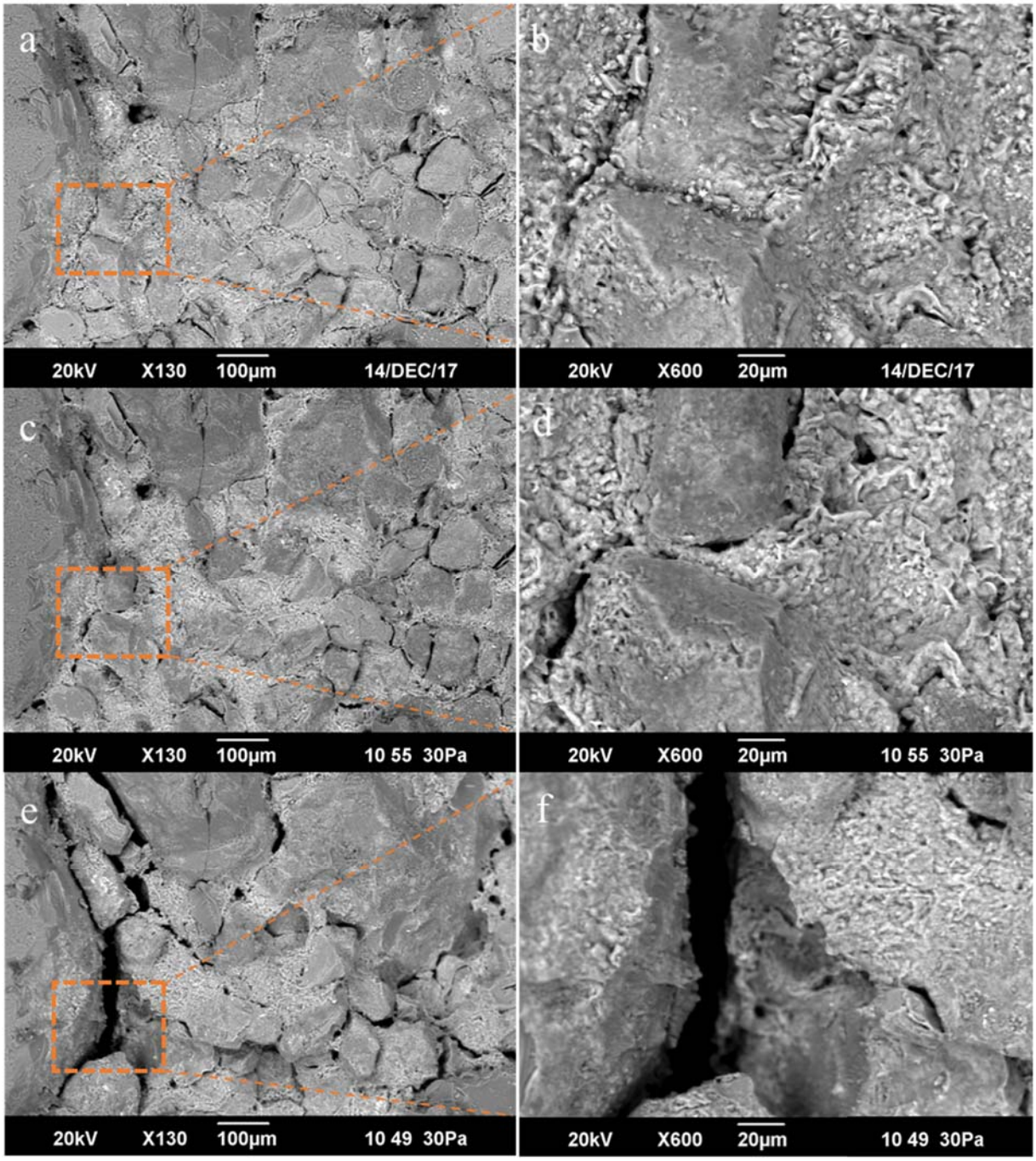

Figure S4: SEM images of MS4 (a,b) initial sample, (c,d) sample aged 4 weeks in N_2-saturated brine, and (e,f) sample aged 8 weeks in N_2-saturated brine. The orange boxes in (a) (c) and (e) are enlarged to examine the grain and clay structure in (b), (d) and (f).

Figure S5 shows the SEM images of the MS2 sample, aged in scCO_2-saturated brine. The sample

exhibits slight clay separation at grain boundaries after 4 weeks, but no grain losses. The sample after 8-weeks was significantly disintegrated and the reference area was lost.

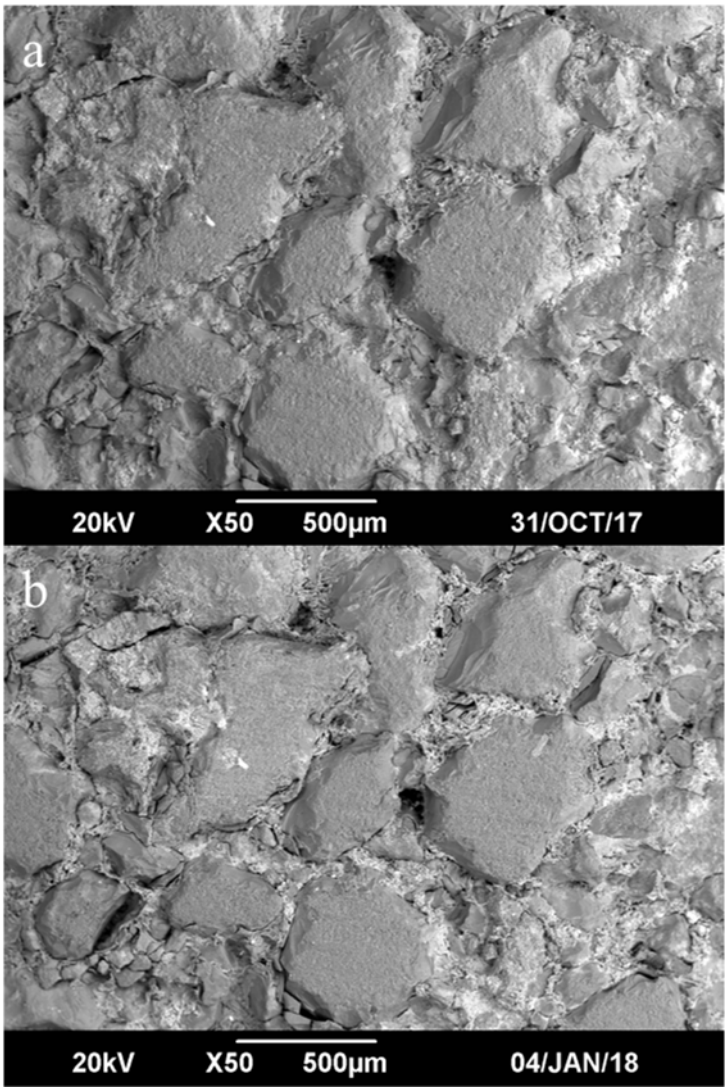

Figure S5: SEM images of MS2 initial (a,b) and 4-week (c,d) sample aged in $scCO_2$–saturated brine. There is slight separation of the clay and grains at grain boundaries and two pores appear larger.

The cation concentrations of Ca, K, Mg, Al, Fe, and Si were analyzed by ICP-OES as indicators of mineral reaction. Concentrations are presented in Figure S6. The concentrations for Ca, K and Mg in replicate samples (a-c) exhibit variation on the same order of changes between the two conditions, and no direct trend could be confirmed. The high total dissolved solid content

of the brine lead to challenges in measuring the lowest concentration ions of Al, Fe, and Si; in order to prevent salting out the plasma torch, the brine was significantly diluted. In most samples, the reported value for Fe, Al, and Si is below the limit of detection for the instrument (1 ppb, with a 100-factor dilution of samples corresponds to 0.1 mg/L). No trend was observed in measured concentrations (d-f).

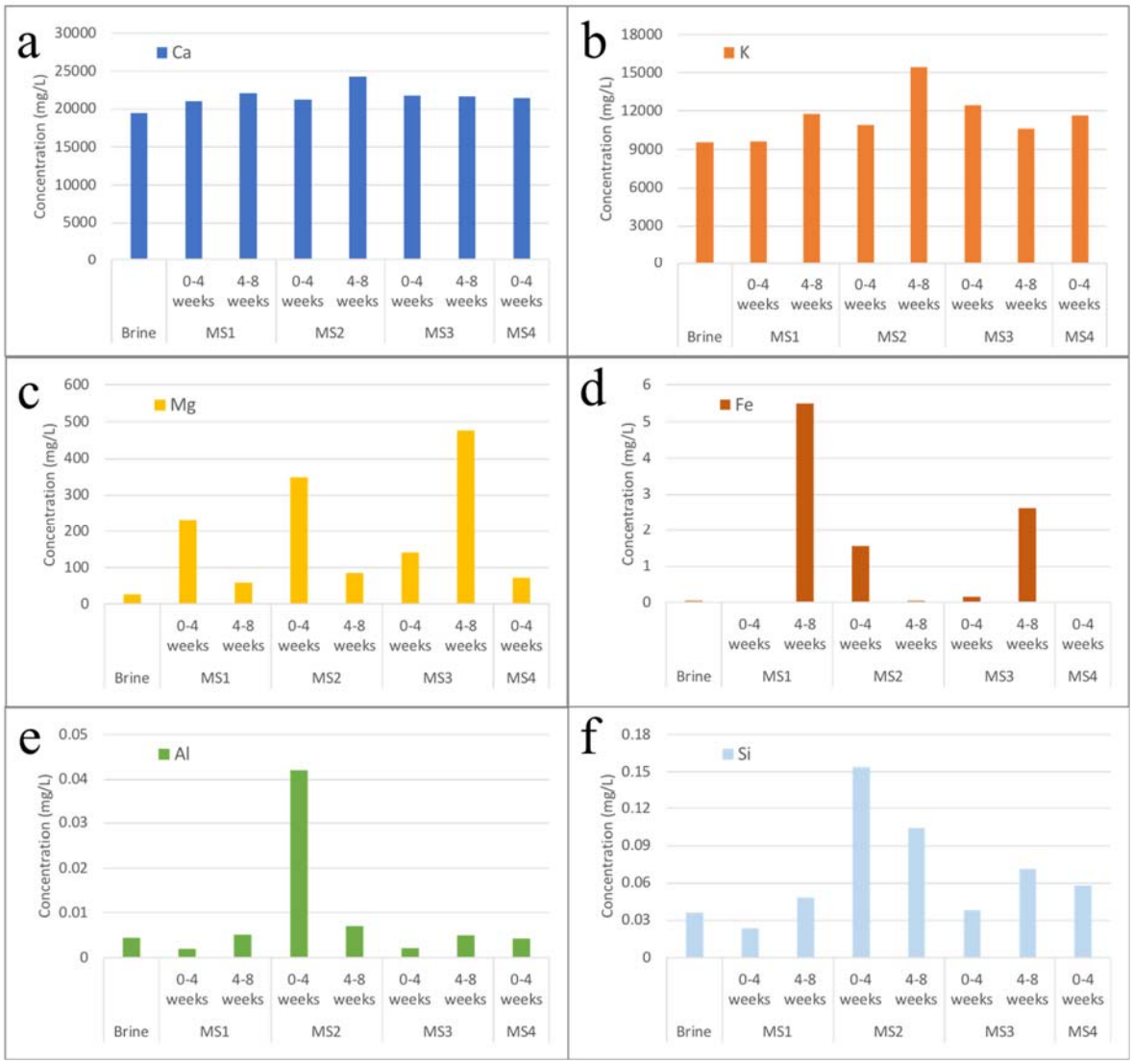

Figure S6: Concentration of cations present in fresh, synthetic brine and subsequent contact with the Mt. Simon and CO_2 or N_2. The brine from MS4 after 8 weeks of aging was not measured. (a)Ca, (b)K, (c) Mg, (d) Fe, (e) Al, and (f) Si are shown under each experimental condition. Only values above 0.1 mg/L are within instrument detection range.

PHREEQC was used to model all ionic components present in solution after brine equilibration with the Mt. Simon sandstone and CO_2 or N_2 at experimental conditions (Figure S7). The final pH for the CO_2 system is 3.9, whereas the N_2 system is 5.9. The concentration values for the N_2 and CO_2 equilibrium states are fairly similar except for C, Ca, Mg, and N, which corresponds to the mineral saturation at those two different pH values. Generally, all samples exhibited lower K concentrations than are present at equilibrium (Figure S6), indicating that concentrations are undersaturated, suggesting further weathering of K-feldspar or cationic exchange in clays will occur with longer aging periods. For the remaining minerals, due to the variability in the results from MS1-MS4, there is no conclusion as to how far the system is from equilibrium.

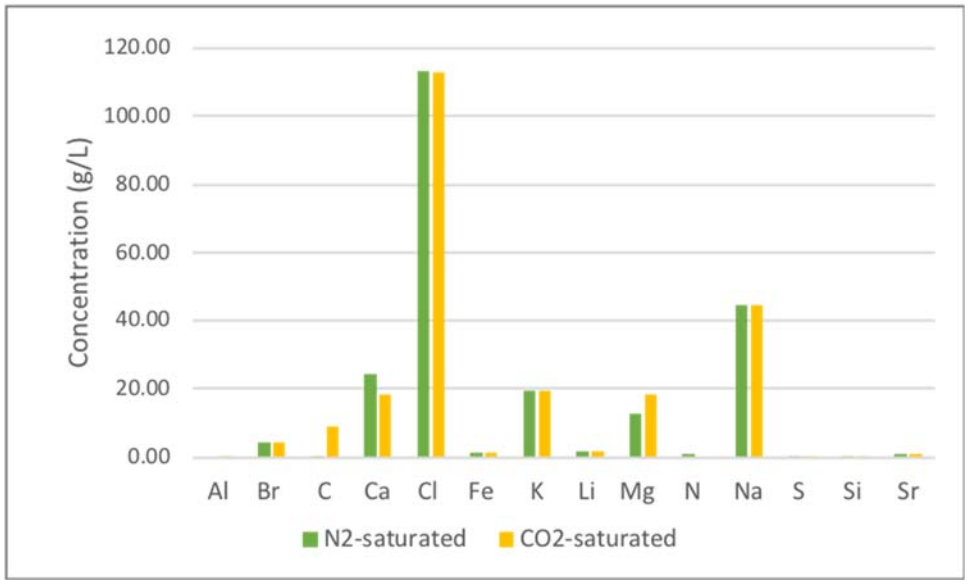

Figure S7: PHREEQC Modeled Equilibrium Concentrations for CO_2 and N_2 with Brine and Mt. Simon sandstone at 52°C and 22 MPa.

References

[1] J. Botto *et al.*, “Effects of Mineral Surface Properties on Supercritical CO2 Wettability in a Siliciclastic Reservoir,” *Energy & Fuels*, p. acs.energyfuels.6b03336, 2017.

[2] D. Barthelmy, “Illite Mineral Data,” 2014. [Online]. Available: http://webmineral.com/data/Illite.shtml#.WOltIFLMz-Y. [Accessed: 09-Apr-2017].

[3] B. B. Bowen *et al.*, “Depositional and diagenetic variability within the Cambrian Mount Simon Sandstone: Implications for carbon dioxide sequestration,” *Environ. Geosci.*, vol. 18, no. 2, pp. 69–89, 2011.